# Hybrid Carbonyl Iron/Iron-Oxide Microfiber Textile Membranes with Magnetically Tunable Capacitance Under Compressive Loading

Ioan Bica , Eugen Mircea Anitas * , Madalin Bunoiu , Liviu Chirigiu , Gabriel Pascu

Posted Date: 23 March 2026

doi: 10.20944/preprints202603.1836.v1

Keywords: magnetodielectric effect; magnetorheological suspension; microwave microplasma; iron oxide microfibers; carbonyl iron; cotton textile composite; planar capacitor

 doi:10.20944/preprints202603.1836.v1



*Article*

# Hybrid Carbonyl Iron/Iron-Oxide Microfiber Textile Membranes with Magnetically Tunable Capacitance Under Compressive Loading

**Ioan Bica [1,2], Eugen Mircea Anitas [2,3,4,*], Madalin Bunoiu [1], Liviu Chirigiu [5] and Gabriel Pascu [1]**

[1] Department of Physics, West University of Timisoara, V. Parvan Avenue 4, 300223 Timisoara, Romania
[2] Department of Physics, Craiova University, A. I. Cuza Street 13, 200585 Craiova, Romania
[3] Joint Institute for Nuclear Research, Joliot-Curie 6, 141980 Dubna, Russia
[4] Horia Hulubei, National Institute of Physics and Nuclear Engineering, 077125 Magurele, Romania
[5] Faculty of Pharmacy, University of Medicine and Pharmacy Craiova, Petru Rares 2, 200349 Craiova, Romania
* Correspondence: anitas@theor.jinr.ru

**Abstract**

Flexible textile membranes were prepared by impregnating woven cotton fabrics with silicone-oil (SO)-based suspensions containing carbonyl iron (CI) microparticles and iron-oxide microfibers ($\mu$Fe). The microfibers were obtained by a microwave-assisted microplasma process and then co-dispersed with CI in SO. In the final membranes, the CI content was kept constant at $\Phi_{CI} = 10$ vol.%, whereas the microfiber fraction was 0, 10 and 20 vol.%. The resulting membranes were used as dielectric layers in planar capacitors and examined at 1 kHz under a static magnetic field of up to 150 mT and compressive pressure up to 10 kPa. In every composition, the capacitance rose with increasing magnetic flux density, but both the zero-field capacitance and the field-induced capacitance change became smaller as the microfiber content increased. A monotonic, nearly linear increase in capacitance was also observed under compression over the tested pressure range. Within a simplified parallel-plate and magnetic-stress analysis, the capacitance data were further used to estimate the apparent relative permittivity, together with capacitance-derived indicators of deformation and stiffness. These estimates suggest field-induced stiffening of the membranes and to a higher apparent low-field stiffness at higher microfiber loading. The obtained hybrid CI/$\mu$Fe microfiber textile membranes can serve as composition-tunable dielectric layers whose electrical response is influenced by both magnetic field and compressive loading, making them relevant for flexible capacitor-based elements.

**Keywords:** magnetodielectric effect; magnetorheological suspension; microwave microplasma; iron oxide microfibers; carbonyl iron; cotton textile composite; planar capacitor

## 1. Introduction

Flexible capacitive sensors are widely used in wearable systems, human–machine interfaces, and robotic sensing because they combine mechanical flexibility, conformability, and low-power operation [1–3]. In the parallel-plate description, the capacitance depends on the electrode area, the electrode spacing, and the apparent relative permittivity $\varepsilon_r$ of the dielectric layer. Mechanical deformation generates an electrical signal by changing one or more of these parameters [1,4]. Therefore, the structure, stiffness, and dielectric response of the dielectric layer largely determine how the sensor deforms under load, and, thus, its sensitivity and operating range [1,4,5]. This has stimulated interest in dielectrics whose response can be tuned by mechanical loading together with additional external stimuli.

Magnetically responsive composites provide one such route. In magnetoactive elastomers and magnetorheological suspensions (MRSs), magnetizable microparticles are dispersed in an electrically

 doi:10.20944/preprints202603.1836.v1



insulating matrix [6,7]. Under a static magnetic field, the particles become magnetized and interact through dipolar forces, promoting chain-like or columnar aggregates aligned with the field [8,9]. This restructuring modifies the internal microgeometry and the local electric-field distribution and is commonly accompanied by a pronounced change in the apparent dielectric response [6,9,10]. Carbonyl iron (CI) microparticles are among the most widely used soft-magnetic fillers in such systems [8,9,11,12].

However, the use of spherical CI microparticles alone can limit the development of lightweight soft dielectrics because their high density tends to reduce sedimentation stability [13]. One way to expand tunability is to introduce a fibrous magnetic phase that restructures the field-responsive architecture without requiring very high filler loadings. For example, replacing spherical fillers with magnetic nanofibers in elastomers promotes interconnected networks and produces strong field-responsive behavior at substantially lower filler contents [14]. More recently, magnetorheological fibrous materials have been shown to exhibit pronounced controlled bending and stiffening by a magnetic field, enabling smart-textile actuation and tunable rigidity [15]. In suspensions, fibrous additives can also reinforce the field-induced structure and improve dispersion stability [16].

Hybrid textile-like composites that combine cotton fibers, CI microparticles, and iron-oxide microfibers ($\mu$Fe) are particularly interesting in this respect. In such systems, the microfiber component can reduce effective density and act as an anti-sedimentation medium, while the dielectric response varies systematically with microfiber fraction and magnetic flux density ($B$) [17]. These behaviors arise due to the changes induced by the microfibers in the spacing and arrangement of CI magnetic dipoles [17]. Microfiber concentration controls both magneto-dielectric and viscoelastic characteristics, and fiber-thread scaffolds can support particle chains and improve shear or damping under field [18,19]. Such results motivate hybrid particle–fiber dielectrics in which the magnetocapacitive response can be tuned through magnetic loading and phase morphology [14,17].

Textile dielectrics are attractive for wearable capacitive devices because they can undergo large reversible thickness changes while maintaining flexibility and, in some cases, high air permeability. [20,21]. Natural fibers such as cotton and cellulose strengthen this approach by offering abundant, skin-friendly scaffolds that can be electrically functionalized. Cellulosic materials are widely used in wearable sensors [22], and cotton fabrics have been modified with conductive electrodes and dielectric additives to improve capacitive performance [23]. However, these textile sensors predominantly rely on mechanically induced capacitance changes, whereas the integration of magnetodielectric tunability into porous textile dielectrics remains comparatively underexplored.

In this work, we fabricate hybrid magneto-responsive textile membranes by impregnating woven cotton scaffolds with silicone-oil (SO)-based suspensions containing CI microparticles and $\mu$Fe. Three membranes with constant CI loading ($\Phi_{CI} = 10$ vol.%) and increasing $\mu$Fe content (0, 10, and 20 vol.%) are integrated as dielectric layers in planar capacitors. Using capacitance measurements at 1 kHz under controlled $B$ and compressive pressure $p$, we estimate the apparent relative permittivity $\varepsilon_r$ and compare trends in magnetic-field sensitivity, pressure response, and apparent field-induced stiffening.

## 2. Materials and Methods

A schematic overview of the fabrication route (particle/fiber preparation, suspension formulation and textile impregnation), capacitor assembly, and magnetic-field-dependent electrical measurements together with the main data-reduction steps is shown in Figure 1. Details for each step are provided in the following subsections.

 doi:10.20944/preprints202603.1836.v1



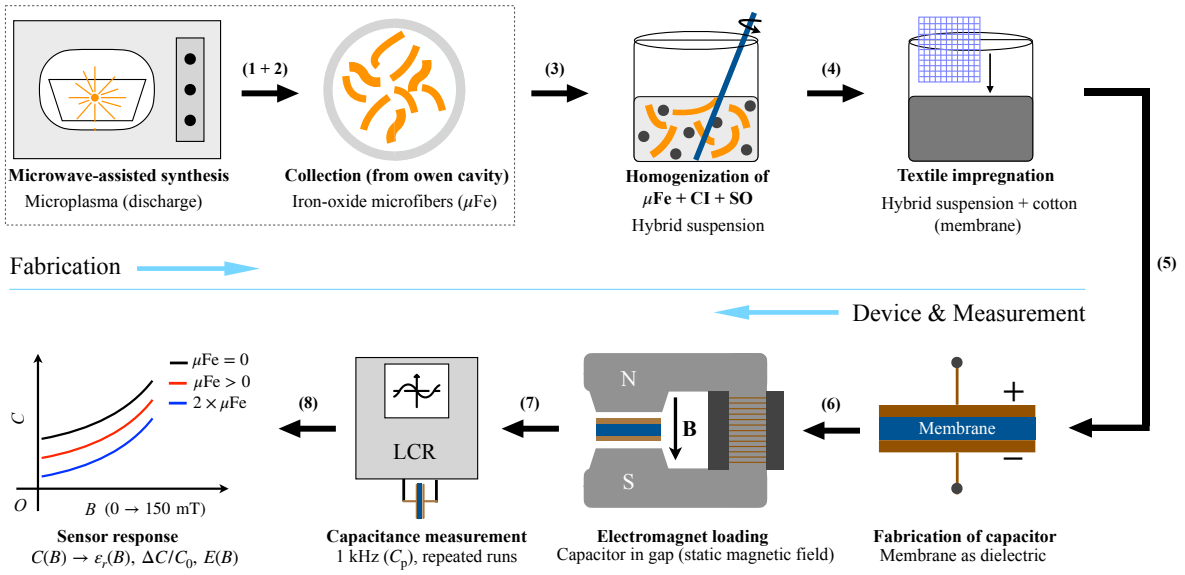


**Figure 1.** Schematic workflow for fabricating (upper row) and testing (lower row) hybrid CI/$\mu$Fe cotton membranes. The two steps enclosed by the dashed frame (microwave-induced microplasma synthesis of $\mu$Fe and their collection) were performed and reported previously in Ref. [24]. In this work, the $\mu$Fe are co-dispersed with CI microparticles in SO to prepare hybrid suspensions, which are then used to impregnate cotton fabric and obtain flexible membranes. The membranes are further assembled as dielectric layers in planar capacitors, exposed to a static magnetic field, and characterized by capacitance measurements at 1 kHz. The capacitance was used to calculate $\varepsilon_r$, the normalized capacitance change, and the apparent modulus-like parameter $E$.

### 2.1. Materials

- CI microparticles, purchased from Sigma-Aldrich, were used as received. According to the supplier, the CI microparticles have a mean diameter of about 5 µm (Appendix A) and a mass density $\rho_{CI} = 7.68$ g/cm$^3$ at 24°C. The specific saturation magnetization is $\sigma_{CI} = 195$ A·m$^2$ / kg, at magnetic field intensities $H \gtrsim 500$ kA/m [25].
- The carrier liquid is SO, grade MS100, used as received (viscosity and density at 24 °C: 100 cSt and, respectively, $\rho_{SO} = 0.98$ g/cm$^3$) [26].
- $\mu$Fe were synthesized in-house as described in Section 2.2 (see also Ref. [24]). Their average diameter is $d_{\mu Fe} \simeq 0.94$ µm and mass density $\rho_{\mu Fe} = 2.875$ g/cm$^3$ at 24 °C. The specific saturation magnetization is $\sigma_{\mu Fe} = 22.7$ A·m$^2$/kg, at $H \gtrsim 500$ kA/m [24].
- Commercial cotton fabric (CF) was used as the porous textile scaffold. The fabric is a woven mesh of interwoven threads. The threads have a diameter $d_t \approx 0.12$ mm and are composed of cotton microfibers with a diameter $d_y \approx 5.5$ µm, leaving spaces that facilitate liquid uptake by capillarity [27].
- FR-4 laminate boards coated with copper (LAM75X100H, Electronic Light, Romania), consisting of an epoxy resin/glass-fiber reinforced substrate with a single-sided copper cladding. The laminate thickness is 0.6 mm and the board size is 100 mm × 75 mm. The nominal thickness of the copper plate is 18 µm.

### 2.2. Synthesis of μFe Microfibers

$\mu$Fe were synthesized using a microwave-assisted microplasma route, following the protocol reported in [24]. Iron pentacarbonyl (Fe(CO)$_5$) served as the iron precursor. A polyphasic precursor mixture consisting of CI microparticles, Fe(CO)$_5$ and SO was homogenized in an open, heat-resistant glass beaker and exposed to microwave irradiation in a domestic microwave oven (2.45 GHz; Samsung MG23F301TAK). The microwave output power and exposure time were set to 450 W and 120 s, respectively, as in Ref. [24]. The precursor composition was identical to Ref. [24] (CI: 2 cm$^3$, Fe(CO)$_5$: 1 cm$^3$, SO: 5 cm$^3$). After microwave treatment, a loose cotton-wool-like product composed of $\mu$Fe was

 doi:10.20944/preprints202603.1836.v1



obtained [24]. After completion of the irradiation step, the product was cooled to room temperature and collected mechanically from the beaker and chamber surfaces. The microfibers collected were stored in sealed glass vials at room temperature until use in hybrid suspensions (Section 2.3). These processes correspond to the first two steps (**1 + 2**), enclosed by the dashed line, in Figure 1.

During microwave irradiation, a luminous microplasma and intermittent micro-explosion-like events can occur in the precursor mixture, promote rapid decomposition of the iron precursor and the formation of transient metal-vapor/gas streams. In cooler regions of the vessel and chamber, these vapors can condense ("dew-point" zones), generating ultrafine iron/iron-oxide particulates that further undergo nonstationary mass transfer and aggregation into a fluffy, cotton-wool-like product. The resulting hierarchical microfiber network is therefore consistent with a vapor–condensation-assembly route occurring under microplasma-assisted microwave heating (see Ref. [24] for a detailed mechanistic discussion and characterization).

### *2.3. Preparation of Hybrid Suspensions*

Hybrid MRSs are prepared by co-dispersing CI microparticles and $\mu$Fe in SO. The volume of the components ($V_{CI}$, $V_{SO}$, $V_{\mu Fe}$) was set to the values specified in Table 1. For each suspension, the corresponding volume fractions are calculated as follows:

$$\Phi_k = \frac{V_k}{V_{CI} + V_{SO} + V_{\mu Fe}}, \qquad k \in \{\text{CI, SO, } \mu\text{Fe}\}. \tag{1}$$

The suspensions were prepared following a common protocol:

**Step 1:** The volumes of CI microparticles, SO, and $\mu$Fe microfibers were measured according to Table 1.

**Step 2:** The measured quantities are introduced into 20 mL Berzelius glass beakers (one beaker per composition).

**Step 3:** Each mixture is homogenized mechanically under heating (warm mixing) for approximately 300 s at about 150°C.

**Step 4:** After the heating stage, thermal treatment is stopped, while mechanical homogenization is continued until the mixture temperature reached ambient temperature. At the end of this step, the MRSs were obtained (step (**3**) in Figure 1) with the volume fractions listed in Table 1.

During preparation, the temperature was monitored using an infrared thermometer (IRT-350 type, Conrad Electronic SE, Germany). The prepared suspensions were used for textile impregnation immediately after preparation.

**Table 1.** Component volumes and volume fractions of CI, SO, and $\mu$Fe used to prepare the hybrid MRSs.

| | $V_{CI}$ (cm$^3$) | $V_{SO}$ (cm$^3$) | $V_{\mu Fe}$ (cm$^3$) | $\Phi_{CI}$ (%vol.) | $\Phi_{SO}$ (%vol.) | $\Phi_{\mu Fe}$ (%vol.) |
|---|---|---|---|---|---|---|
| $MRS_1$ | 0.800 | 3.200 | 0.000 | 20 | 80 | 0 |
| $MRS_2$ | 0.800 | 2.800 | 0.400 | 20 | 70 | 10 |
| $MRS_3$ | 0.800 | 2.400 | 0.800 | 20 | 60 | 20 |

### *2.4. Fabrication of Hybrid Cotton Membranes*

Hybrid CI/$\mu$Fe cotton membranes were manufactured by impregnating CF with freshly prepared hybrid $MRS_1$–$MRS_3$. Square CF specimens with a side length of 30 mm were cut from the same fabric roll. For each composition, a CF sample was placed in a 20 mL Berzelius glass beaker and impregnated with the corresponding suspension by adding an equal amount of aliquot (sufficient to fully wet/submerge the textile) and allowing capillarity uptake.

To promote infiltration into the textile network and improve the uniformity of the dispersion, each beaker containing the CF sample and suspension was subjected to a short warm treatment

 doi:10.20944/preprints202603.1836.v1



(approximately 300 s) while mechanically agitated. The beakers were then allowed to cool to ambient temperature. The impregnated samples were left to equilibrate at room temperature for 24 h. After this period, the resulting membranes were removed and placed above a Petri dish (or on an inert support) to allow removal of visible excess liquid by gravitational draining.

The membranes were labeled according to the suspension used for impregnation: $hM_1$ (from $MRS_1$), $hM_2$ (from $MRS_2$) and $hM_3$ (from $MRS_3$). The CI loading was kept constant in the MRSs at $\Phi_{CI} = 20$ vol.% (Table 1). After impregnation, the volume fractions of the membrane change because the cotton scaffold contributes an additional volume. Consequently, the volume fraction of CI in the membranes is $\Phi_{CI} = 10$ vol.% for all samples (Table 2). The membrane thickness measured after draining was approximately the same for all three compositions, namely $d \approx 0.42$ mm. The membranes were stored in sealed containers at room temperature until the capacitor assembly (Section 2.5).

Hybrid membranes ($hM_i$, $i = 1, 2, 3$) obtained by cotton impregnation (Figure 2) have the compositions summarized in Table 2. This corresponds to step (**4**) in Figure 1. For each membrane, the volumes of the components (CI, SO, CF scaffold and $\mu$Fe) and the corresponding volume fractions are reported.

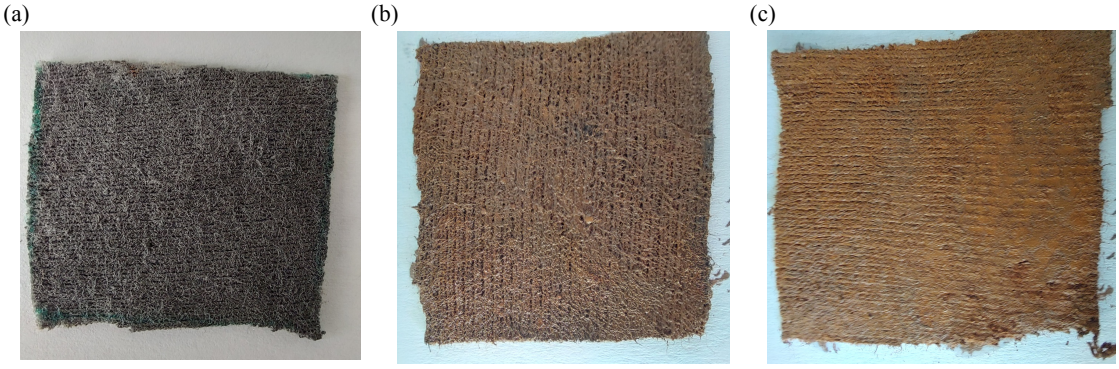


**Figure 2.** Photographs of the hybrid membranes prepared with increasing $\mu$Fe loading. (a) $hM_1$. (b) $hM_2$. (c) $hM_3$. The membrane color changes from black ($hM_1$) to progressively more brownish tones at higher $\mu$Fe content. The edge of each membrane is 30 mm.

**Table 2.** Component volumes and volume fractions of CI, SO, CF, and $\mu$Fe in the hybrid membranes $hM_i$ (i=1,2,3).

| | $V_{CI}$ ($cm^3$) | $V_{SO}$ ($cm^3$) | $V_{\mu Fe}$ ($cm^3$) | $V_{CF}$ ($cm^3$) | $\Phi_{CI}$ (%vol.) | $\Phi_{SO}$ (%vol.) | $\Phi_{\mu Fe}$ (%vol.) | $\Phi_{CF}$ (%vol.) |
|---|---|---|---|---|---|---|---|---|
| $hM_1$ | 0.072 | 0.288 | 0.000 | 0.360 | 10 | 40 | 0 | 50 |
| $hM_2$ | 0.072 | 0.216 | 0.072 | 0.360 | 10 | 30 | 10 | 50 |
| $hM_3$ | 0.072 | 0.144 | 0.144 | 0.360 | 10 | 20 | 20 | 50 |

### *2.5. Planar Capacitor Assembly*

Hybrid membranes $hM_i$ (i=1,2,3) were used as dielectric layers in parallel capacitors $PC_i$ (i = 1,2,3) manufactured from single-sided copper-clad FR-4 boards. The copper cladding served as the electrode material. For each capacitor, two identical electrodes were prepared and arranged face-to-face, with the membrane placed between them. The electrode overlap area $A$ was defined by the geometry of the copper pad (Figure 3a) and was kept constant for all measurements. Here, it corresponded to a square region of 30 mm $\times$ 30 mm. Then, each membrane was centered on the lower electrode so that the overlap area was fully covered by the membrane. The upper electrode was then aligned to ensure a reproducible overlap area and to minimize lateral misalignment. This corresponds to step (**5**) in Figure 1.

The capacitor stack (FR-4/copper electrode–membrane–copper electrode/FR-4) was laterally aligned and enclosed using an insulating adhesive tape (3M) to ensure reproducible positioning and mechanical integrity (Figure 3a). The tape helped maintain the alignment of the stack and provided a

 doi:10.20944/preprints202603.1836.v1



mild mechanical restraint. The electrical connection to the copper electrodes was made using insulated leads attached to the electrodes (Figure 3b).

The total thickness of the capacitor (including the supports and FR-4 tape) was approximately 6 mm; however, in the capacitance analysis the effective separation of the electrode was taken as the membrane thickness $d$ measured by micrometer. Representative photos of the assembled device are shown in Figure 3(c).

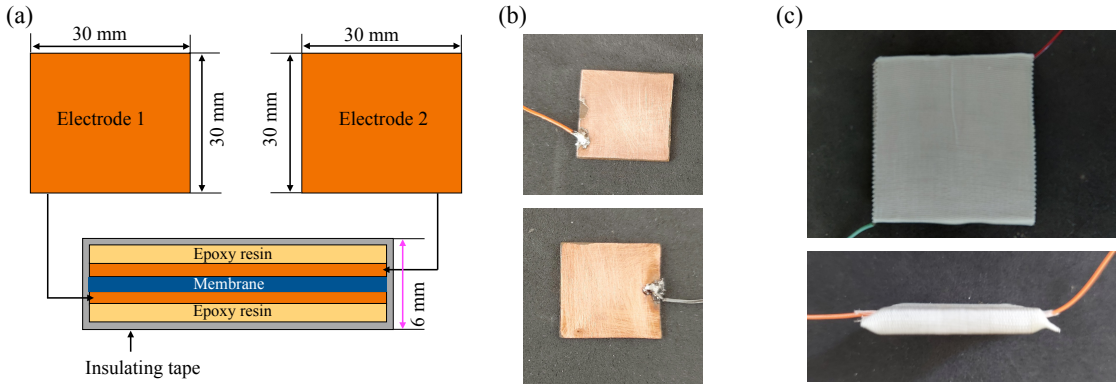


**Figure 3.** Planar capacitor design and assembly used for capacitance measurements. (a) Schematic of the device: top—plan view of the two copper electrodes; bottom—cross-sectional stack (not to scale) comprising FR-4/epoxy substrate–copper electrode–hybrid membrane–copper electrode–FR-4/epoxy substrate, enclosed and laterally aligned using insulating adhesive tape. (b) Photographs of the individual electrodes with attached electrical leads. (c) Photographs of the assembled capacitor: top—top view of the taped device with the two electrical connections; bottom—side/cross-sectional view showing the stacked configuration.

### *2.6. Magnetic-Field Setup and Electrical Measurements*

Capacitance measurements were performed with the planar capacitor (Section 2.5) placed in the air gap between the N and S poles of a custom-built electromagnet (EM). This corresponds to step (**6**) in Figure 1. EM consists of a coil (Figure 4, position 1) wound on a ferromagnetic yoke (Figure 4, position 2). The pole gap was set at 6 mm. The coil was powered in direct-current source (DCS) mode by a regulated power supply (RXN-3020D, Rexton Electronics Co. Ltd., China), allowing continuous tuning of $B$ up to $\approx$ 150 mT.

The $B$ in the sample region was monitored using a gaussmeter (Dexing Magnet, China) equipped with a Hall probe (Figure 4, Hs). During measurements, the Hall probe was positioned beneath the capacitor stack, aligned with the center of the electrode overlap area, to provide a reproducible reading of the local magnetic field experienced by the sample.

Capacitance was measured using an inductance-capacitance-resistance (LCR) bridge (CHY-41R, Taiwan–China) connected to the capacitor electrodes (Figure 4, Br). This corresponds to step (**7**) in Figure 1. Measurements were performed at a fixed frequency of 1 kHz in a parallel equivalent-circuit configuration appropriate for a planar capacitor.

 doi:10.20944/preprints202603.1836.v1



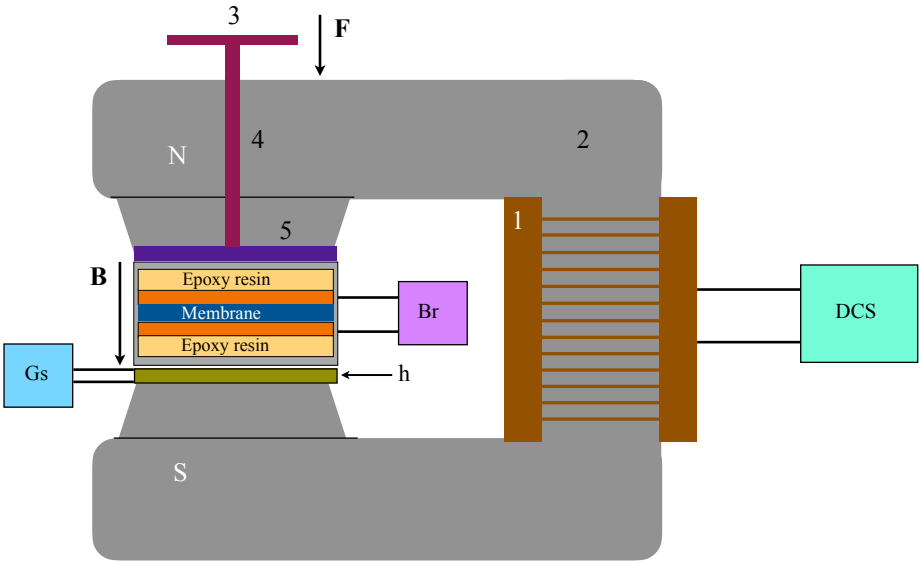


**Figure 4.** Schematic of the experimental setup used to apply a static magnetic field and a controlled normal load to the planar capacitor. The custom-built EM comprises the coil (1) and magnetic yoke (2), driven by a DCS power supply. The capacitor stack is positioned in the pole gap and connected to the LCR bridge (Br) for capacitance measurements. $B$ in the sample region is monitored using a Hall probe (Hs) placed beneath the stack and read out by a gaussmeter (Gs). The assembly is mounted on a textolite support plate (3) and aligned using a brass rod (4, diameter 8 mm) and a brass plate (thickness 1.5 mm).

In addition to the magnetic field, a controlled normal load could be applied to the capacitor stack along the direction of the magnetic field (Figure 4). A vertical hole drilled through the yoke allows a loading rod to pass. Masses (m) are placed on the loading platform to generate a compressive force $F = mg$, corresponding to $p = F/A$, where $A$ is the area of overlap of the electrode (Section 2.5). For each membrane, the capacitor was mounted in the EM gap using identical positioning and tapping conditions. The magnetic field was set by adjusting the DCS current supplied to the coil, and the corresponding value $B$ was read from the gaussmeter.

From the measured field and load-dependent capacitance, we subsequently determined $\varepsilon_r$ of the membranes, the magnetic stress ($\tau_{zz}$), the apparent strain ($e_{zz}$), and the apparent modulus-like parameter ($E$) as described in Section 2.7. This corresponds to step (**8**) in Figure 1.

### *2.7. Data reduction and extracted quantities*

For each membrane ($hM_i$, $i = 1, 2, 3$), the equivalent capacitance $C(B, p)$ of the planar capacitor (Section 2.5) was measured at $f = 1$ kHz (Section 2.6) as a function of $B$ and $p$.

To quantify the magnetic-field-induced capacitance change, we define the magnetocapacitance as

$$\mathrm{MC}(B, p) = \frac{C(B, p) - C(0, p)}{C(0, p)} \times 100\%. \tag{2}$$

Here, $C(B, p)$ is the capacitance measured at $B$ and $p$, while $C(0, p)$ is the corresponding zero-field capacitance measured at the same $p$.

To quantify pressure-sensing performance, we define the average normalized pressure sensitivity as

$$S_p(B) = \frac{[C(B, p_{\max}) - C(B, 0)]/C(B, 0)}{p_{\max}}, \tag{3}$$

where $C(B, 0)$ is the capacitance at $p = 0$ kPa, $C(B, p_{\max})$ is the capacitance at maximum applied pressure $p_{\max}$, and $S_p(B)$ represents the average normalized pressure sensitivity over $0 \le p \le p_{\max}$.

The quantities directly measured are the capacitances at the device-level $C(B, p)$ of the assembled capacitor structures. The dielectric and mechanical-response quantities introduced in the following are model-derived effective or apparent parameters. Although the primary observables are $C(B, p)$

 doi:10.20944/preprints202603.1836.v1



of the assembled capacitor, the quantities reported below are attributed to the hybrid membrane within a simplified description of effective-medium. In this framework, the field- and load-dependent response is assumed to be dominated by the dielectric layer, while the electrodes and supports are treated as geometrically and electrically invariant. Consequently, $\varepsilon_r$ is used here as an apparent relative permittivity, $e_{zz}$ as a capacitance-derived proxy, and $E$ as an apparent modulus-like parameter derived within the adopted magnetic-stress model.

Using the parallel-plate capacitor relation, $\varepsilon_r$ of membrane $i$ ($i = 1, 2, 3$) at a given $B$ was calculated using the zero-field thickness as

$$\varepsilon_r(B) = \frac{C(B,0)\, d}{\varepsilon_0\, A}, \tag{4}$$

where $\varepsilon_0$ is the vacuum permittivity, $A$ is the electrode overlap area, and $d$ is the membrane thickness. For the present capacitors, $A \equiv L^2$, $L = 30$ mm (see Figure 3) and $d = 0.42$ mm. Unless stated otherwise, $\varepsilon_r(B)$ is evaluated at $p = 0$. Because the membrane thickness may change under magnetic field and the dielectric layer is structurally heterogeneous, $\varepsilon_r(B)$ obtained in this way is an apparent effective quantity.

Because the measured capacitance increases under a magnetic field, the field-induced deformation is assumed to be predominantly compressive. To obtain a comparative measure of deformation from capacitance data, we estimate [28]

$$e_{zz} = \frac{C(0,p)}{C(B,p)} - 1, \tag{5}$$

where $C(0,p)$ and $C(B,p)$ are the capacitances measured at the same $p$ in the absence and presence of a magnetic field, respectively.

Following the dipolar interaction approximation adopted in [29], the magnetic interaction force acting on the membrane can be approximated as

$$F_m \approx -9\Phi_{CI} L^2 B^2/(2\mu_0), \tag{6}$$

from which we obtain:

$$\tau_{zz} = F_m/L^2 \approx -9\Phi_{CI} B^2/(2\mu_0). \tag{7}$$

In the following mechanical analysis, $\Phi_{CI}$ refers to the volume fraction of CI microparticles in the final membrane (Table 2), not in the precursor suspension (Table 1). Therefore, for the membranes investigated here, $\Phi_{CI} = 10$ vol.% and $\mu_0 = 4\pi \times 10^{-7}$ H/m, so Equation (7) becomes:

$$\tau_{zz}(\text{Pa}) \approx -0.358\, B^2(\text{mT}). \tag{8}$$

The negative sign indicates that the membranes undergo compression in the applied magnetic field.

An apparent modulus-like parameter of each membrane can then estimated from the ratio between$\tau_{zz}$ and field-induced strain:

$$E = \frac{\tau_{zz}}{e_{zz}}. \tag{9}$$

Because $\tau_{zz}$ is estimated from a simplified dipolar magnetic-stress model and $e_{zz}$ is indirectly inferred from capacitance, $E$ should be interpreted here as an apparent comparative stiffness indicator.

## 3. Results

### *3.1. Morphology, Composition, and Magnetic Properties of μFe*

The morphology, composition, phase constitution, and magnetic properties of the $\mu$Fe used here were previously established in [24]; only a brief summary is given because these characteristics define the secondary magnetic filler in the hybrid CI/$\mu$Fe membranes. Scanning electron microscopy (SEM) observations showed that the microwave-synthesized microfibers form a complex hierarchical spiderweb-like network of interconnected filaments, with diameters in the range of approximately 0.25–2.20 μm and an average diameter of about 0.94 μm [24]. Energy-dispersive X-ray spectroscopy (EDX)

 doi:10.20944/preprints202603.1836.v1



analysis confirmed that the microfibers contain Fe and O, while X-ray diffraction (XRD) measurements revealed a mixed-phase iron-oxide composition consisting of $\alpha$-$Fe_2O_3$, $\gamma$-$Fe_2O_3$, and $Fe_3O_4$ [24].

Room-temperature magnetic measurements further showed that the microfibers are magnetically active, with a specific saturation magnetization of $\sigma_{\mu Fe} \approx 22.7$ A·m $^2$ / kg, a remanent magnetization of approximately 2.86 A·m$^2$/kg, and a coercive field of approximately 12.3 kA/m [24]. These values are substantially lower than those of CI microparticles (see Appendix A), which is consistent with the mixed-phase oxidized nature of the microfibers. At the same time, the hierarchical morphology and mixed iron-oxide composition of the $\mu$Fe provide structural and magnetic features that are complementary, rather than redundant, to those of CI. Therefore, when incorporated together with CI in cotton-based membranes, $\mu$Fe are expected to act as a secondary magnetic filler that modifies the packing of particles, constrains the field-induced rearrangement and thereby helps tune the dielectric and apparent mechanical response of the hybrid CI/$\mu$ Fe textile membranes investigated here.

### *3.2. Membrane Morphology and Structure*

To study the morphology and structure, a SEM Inspect S PANalytical model from FEI Company (Eindhoven, The Netherlands) was used in low-vacuum mode and high voltage of 30.00 kV, coupled with EDX analysis detector with energies generated up to about 12 keV. Representative SEM images and EDX spectra of the pure cotton fabric and of a hybrid CI/$\mu$ Fe membrane fabricated are shown in Figure 5. The pristine cotton fabric exhibits the expected interconnected fibrous architecture, with individual microfibers forming an open scaffold that contains voids suitable for suspension uptake during membrane fabrication. This morphology is consistent with the role of the textile as a flexible porous support for the magnetic filler dispersed in silicone oil.

After impregnation, the membrane preserves the overall fibrous texture of the cotton scaffold, but the SEM image reveals additional solid-phase features associated with the incorporated magnetic filler. Compared to pristine fabric, the membrane appears denser and less open, indicating that the CI microparticles and $\mu$Fe are distributed within and around the cotton-fiber network. The corresponding EDX spectrum further confirms the presence of Fe-containing inorganic material in the membrane, demonstrating successful incorporation of the magnetic phase into the textile structure. In general, the SEM/EDX observations show that the hybrid membranes retain the flexible fibrous framework related to the cotton substrate.

 doi:10.20944/preprints202603.1836.v1



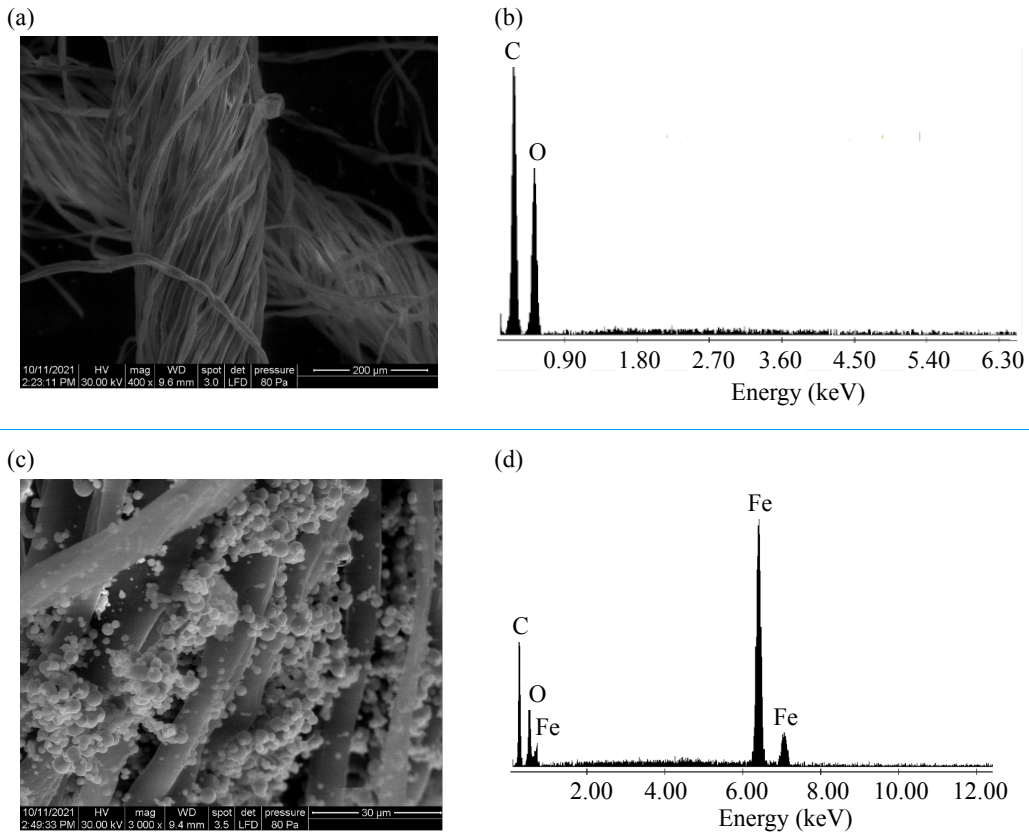


**Figure 5.** Representative SEM images and EDX spectra of (a, b) the pristine cotton fabric and (c, d) the hybrid CI/$\mu$Fe membrane $hM_3$.

### *3.3. Capacitance*

The performance of membrane-based capacitors fabricated as flexible capacitive elements was first assessed by direct electrical measurements under magnetic and mechanical stimuli. For this purpose, the capacitance of the three planar capacitors $PC_1$-$PC_3$ was recorded as a function of $B$ at $p = 0$ kPa (Figure 6a), as a function of $p$ at $B = 0$ mT (Figure 6b), and during magnetic field cycling to examine hysteresis effects (Figure A2 in Appendix B).

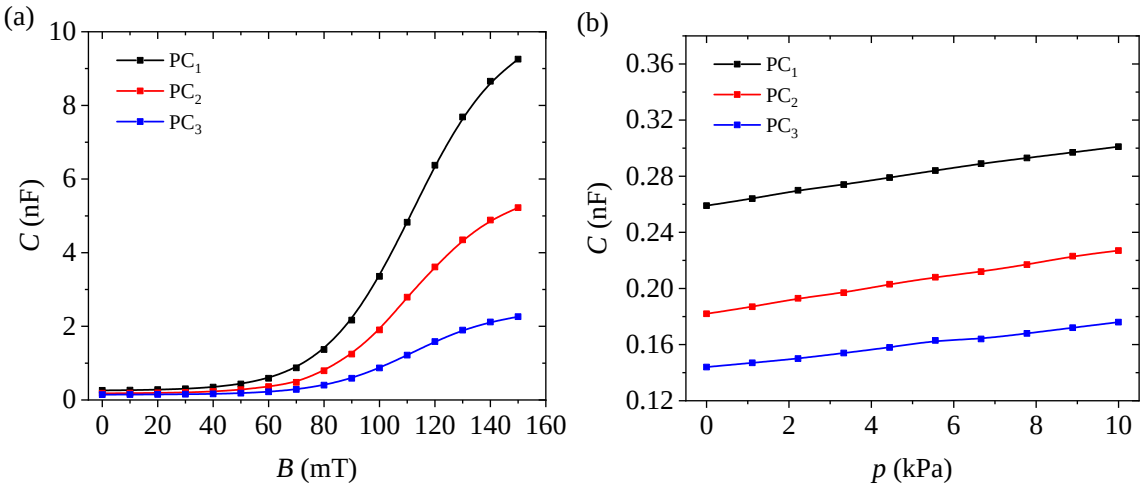


**Figure 6.** Capacitance response of the three planar capacitors based on hybrid CI/$\mu$Fe cotton membranes under magnetic and mechanical stimuli. (**a**) Capacitance, $C$, as a function of $B$, measured at $p = 0$ kPa. (**b**) Capacitance, $C$, as a function of $p$, measured at $B = 0$ mT. Points - experimental data. Continuous lines - interpolation.

 doi:10.20944/preprints202603.1836.v1



The capacitance of all three planar capacitors increased monotonically with $B$ in the investigated range 0–150 mT. In zero field, the capacitance values were 0.259 nF, 0.182 nF, and 0.145 nF for $PC_1$, $PC_2$, and $PC_3$, respectively, and this ordering was preserved throughout the magnetic-field range. The increase was weak at low magnetic flux densities and became much more pronounced above about 60–80 mT, indicating a strongly nonlinear magnetic response. At $B = 150$ mT, the capacitance reached 9.255 nF for $PC_1$, 5.222 nF for $PC_2$, and 2.261 nF for $PC_3$, corresponding to increases of approximately 35.7, 28.7, and 15.6 times relative to their zero-field values.

A monotonic increase in capacitance was also observed with $p$. In the investigated interval 0–10 kPa, the capacitance is quasi-linear for all three capacitors. It increased from 0.259 to 0.301 nF for $PC_1$, from 0.182 to 0.227 nF for $PC_2$, and from 0.145 to 0.176 nF for $PC_3$. These changes correspond to relative increases of approximately 16.2%, 24.7%, and 21.4%, respectively. Although $PC_1$ retained the highest absolute capacitance throughout the pressure range, $PC_2$ displayed the largest absolute and relative pressure-induced increase. The data show that the three capacitor structures are sensitive to both magnetic field and compressive-pressure stimuli, with a much stronger absolute response to the magnetic field than to mechanical loading in the tested ranges.

For a compact comparison of the sensing characteristics, the main metrics extracted from $C(B)$ and $C(p)$ are summarized in Table 3.

**Table 3.** Selected sensor-related metrics of the three planar capacitors, extracted from the capacitance dependences $C(B)$ and $C(p)$. Here, $C_0$ is the capacitance at $B = 0$ and $p = 0$, $C_{150}$ is the capacitance at $B = 150$ mT and $p = 0$, and $C_{10}$ is the capacitance at $p = 10$ kPa and $B = 0$. The magnetocapacitance at the maximum magnetic field, $MC(150\ mT, 0)$, was calculated using Eq. (2). The quantity $\Delta C_p = C_{10} - C_0$ denotes the absolute capacitance change induced by $p$, while the pressure sensitivity $S_p(0)$ was calculated using Eq. (3).

| Sample | $C_0$ | Magnetic-field response | | Pressure response | | |
|---|---|---|---|---|---|---|
| | (nF) | $C_{150}$ (nF) | $MC(150\ mT, 0)$ (%) | $C_{10}$ (nF) | $\Delta C_p$ (nF) | $S_p(0)$ ($kPa^{-1}$) |
| $PC_1$ | 0.259 | 9.255 | 3473.4 | 0.301 | 0.042 | 0.0162 |
| $PC_2$ | 0.182 | 5.222 | 2769.2 | 0.227 | 0.045 | 0.0247 |
| $PC_3$ | 0.145 | 2.261 | 1459.3 | 0.176 | 0.031 | 0.0214 |

### *3.4. Magnetic-Field Dependences of Apparent Relative Permittivity and Apparent Strain*

The capacitance data were further used to evaluate $\varepsilon_r$, and the capacitance-derived proxy $e_{zz}$, as functions of $B$. The corresponding results were calculated using Equations (4) and (5) and are presented in Figure 7. $\varepsilon_r$ increases monotonically with the $B$ for all three membranes, while the $e_{zz}$ component becomes progressively more negative. In both cases, the magnitude of the response decreases in the order $hM_1 > hM_2 > hM_3$. For low magnetic fields, the variations of $\varepsilon_r$ and $e_{zz}$ are relatively weak, whereas much stronger changes occur in the intermediate and high-field range, followed by a tendency toward saturation at the highest values of $B$. At $B = 150$ mT, $\varepsilon_r$ reaches approximately 488.8, 275.0, and 118.5 for $hM_1$, $hM_2$, and $hM_3$, respectively, while $e_{zz} \approx -0.972$, $-0.965$, and $-0.936$.

 doi:10.20944/preprints202603.1836.v1



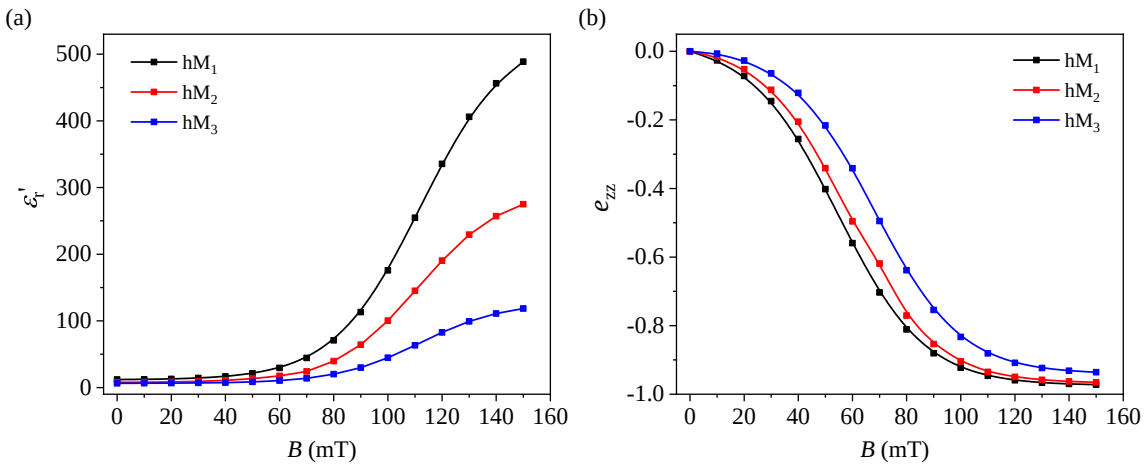


**Figure 7.** Magnetic-field dependences of (**a**) $\varepsilon_r$, calculated with Eq. (4), and (**b**) $e_{zz}$, calculated with Eq. (5), for membranes $hM_1$, $hM_2$, and $hM_3$.

### *3.5. Magnetic Stress and Apparent Modulus-like Response*

$\tau_{zz}$ calculated from Equation (8) and the corresponding apparent modulus-like parameter $E$ (kPa) are shown in Figure 8. As expected from Equation (8), the normal $\tau_{zz}$ is compressive and becomes increasingly negative with increasing $B$, changing from $\tau_{zz} = 0$ at $B = 0$ to $\tau_{zz} \approx -8.06$ kPa at $B = 150$ mT. The magnitude of $\tau_{zz}$ increases nonlinearly throughout the investigated field range, reflecting its approximately quadratic dependence on $B$.

The apparent modulus-like parameter exhibits a membrane-dependent behavior at low and intermediate magnetic fields, followed by a clear increase at higher fields for all three membranes. At $B = 10$ mT, the apparent modulus values are approximately 1.38, 2.23, and 5.29 for $hM_1$, $hM_2$, and $hM_3$, respectively, indicating that $hM_3$ is the most rigid membrane in the low-field range. For $hM_1$, $E$ gradually increases from approximately 1.38 at 10 mT to 8.29 at 150 mT. For $hM_2$, $E$ increases from about 2.23 at 10 mT to 8.35 at 150 mT, with a weak minimum around 50–60 mT. For $hM_3$, the modulus is initially the highest, decreases from about 5.32 at 20 mT to about 3.54 at 70 mT, and then increases again to about 8.61 at 150 mT. At the highest applied field, the apparent modulus values are close for all three membranes, ordering $hM_3 > hM_2 > hM_1$.

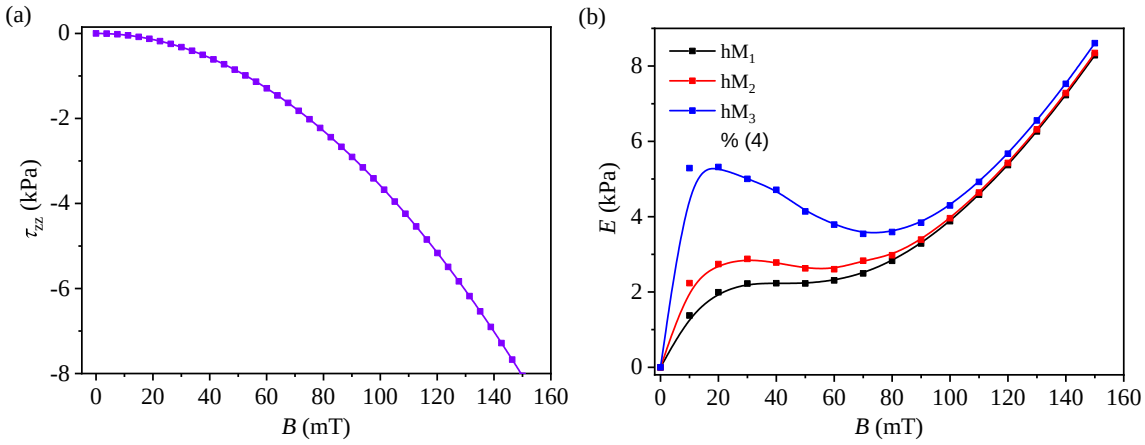


**Figure 8.** Magnetic-field dependences of (**a**) $\tau_{zz}$, calculated from Equation (8), and (**b**) the apparent modulus-like parameter, $E$ (kPa), for membranes $hM_1$, $hM_2$, and $hM_3$, calculated from Eq. (9).

For a compact sensor-oriented comparison, the selected dielectric and apparent mechanical metrics derived from the membranes $hM_1$, $hM_2$, and $hM_3$ are summarized in Table 4. The values show that $hM_1$ has the highest $\varepsilon_r$ and magnetocapacitance, while $hM_3$ exhibits the lowest dielectric response and the highest apparent modulus-like parameter in the intermediate magnetic field. $e_{zz}$ at

 doi:10.20944/preprints202603.1836.v1



$B = 150$ mT remains strongly negative for all three membranes, while the apparent stiffening ratio decreases from $hM_1$ to $hM_3$.

**Table 4.** Representative derived apparent dielectric and mechanical-response metrics of membranes $hM_1$, $hM_2$, and $hM_3$ under magnetic field. Here, $\varepsilon_{r,0}$ is the apparent relative permittivity at $B = 0$, $\varepsilon_r(150)$ and $e_{zz}(150)$ are the corresponding values at $B = 150$ mT, and $R_E = E(150)/E(50)$ is the apparent stiffening ratio. Here $E$ is reported in kPa.

| Membrane | $\varepsilon_{r,0}$ | $\varepsilon_r(150)$ | $e_{zz}(150)$ | $E(50)$ | $E(150)$ | $R_E$ |
|---|---|---|---|---|---|---|
| $hM_1$ | 13.65 | 488.796 | -0.9720 | 2.2272 | 8.2869 | 3.72 |
| $hM_2$ | 9.59 | 275.035 | -0.9652 | 2.6279 | 8.3459 | 3.18 |
| $hM_3$ | 7.64 | 118.529 | -0.9359 | 4.1394 | 8.6070 | 2.08 |

## 4. Discussion

### *4.1. Origin of the Magnetic-Field-Induced Dielectric Response*

Both $C$ and $\varepsilon_r$ increase monotonically with $B$ for all membranes (Figures 6a and 7a). In the present planar-capacitor configuration, this behavior is consistent with the magnetic-field-induced restructuring of the CI-rich phase and the resulting change in the electrical response of the heterogeneous dielectric layer [29,30]. Under an applied magnetic field, the CI microparticles become magnetized and tend to interact along the field direction, which is expected to promote the development of field-induced structures within the cotton scaffold impregnated with SO [30–32].

The response is distinctly nonlinear. At low field the capacitance changes only slightly and then rises much more rapidly in the intermediate range, before approaching saturation at the highest fields. This progression is consistent with the field-induced structuring within the membrane [30]. At low $B$, only limited rearrangement is expected, while at higher $B$ the magnetic interactions become strong enough to induce a much larger change in the internal configuration of the membrane. The smaller incremental variation observed at the highest fields suggests that the system approaches a near-saturated state, so that further increases in $B$ produce only modest dielectric changes.

The simultaneous evolution of $\varepsilon_r$ and $e_{zz}$ further indicates that the dielectric response is coupled to the apparent compressive deformation. As the magnetic field increases, $\varepsilon_r$ increases, while $e_{zz}$ becomes increasingly negative. This indicates that the dielectric enhancement is linked both to changes in the polarization pathways and to field-induced changes in the internal geometry of the composite layer.

### *4.2. Effect of μFe Loading on Magnetocapacitance and Apparent Deformation*

As the fraction of $\mu$Fe increases, the zero-field capacitance decreases, the magnetic-field-induced capacitance change decreases, and $\varepsilon_r$ in a given field is reduced (Figures 6a and 7a). The same trend is observed for the magnitude of $e_{zz}$: at $B = 150$ mT, the absolute value of $e_{zz}$ is highest for $hM_1$ and lowest for $hM_3$ (Figure 7b). Therefore, increasing the $\mu$Fe content reduces both the magnetocapacitance and the magnitude of the apparent deformation derived from the capacitance.

A simple way to interpret these results is to treat the CI-rich phase in the porous textile as a chain-like structure embedded in an oxide-/polymer-/oil-rich dielectric background. In such a microstructural view, the device-level capacitance reflects the combined contribution of many local CI–dielectric–CI interfaces arranged in series/parallel within the electrode overlap area. Increasing the fraction of $\mu$Fe introduces an additional fibrous network rich in iron-oxides that (i) changes the packing and connectivity of the CI-rich domains and (ii) increases the fraction of low/weakly polarizable regions participating in the effective dielectric pathway. Both effects act to lower the zero-field capacitance and to limit the field-induced reconfiguration of the CI-rich phase, thereby reducing the overall magnetocapacitive response. The added fibrous phase can mechanically constrain the rearrangement of the CI-rich domains, consistent with the observed increase in apparent low-field stiffness at higher $\mu$Fe loading.

 doi:10.20944/preprints202603.1836.v1



This behavior is consistent with the different roles played by the two magnetic components. CI remains the dominant magnetically active phase in the membranes because its saturation magnetization is much higher than that of the $\mu$Fe (Section 2.1; Ref. [24]). In contrast, $\mu$Fe, due to their lower magnetization and fibrillar morphology, appear to act mainly as a secondary structural component that modifies the internal spatial arrangement of the composite. A higher $\mu$Fe loading would then be expected to modify or hinder the field-induced chain-like structure of the CI-rich phase and thereby alter the field-responsive performance, while also improving dispersion stability through steric/structural effects [33]. The SEM observations are qualitatively consistent with this view. After impregnation, the cotton scaffold retains its fibrous character, but the membrane becomes denser and contains Fe-rich solid material distributed throughout the textile network (Figure 5).

### *4.3. Apparent Mechanical Response and Field-Induced Stiffening*

The apparent modulus-like parameter $E$ derived increases overall with $B$ for all three membranes, although the detailed behavior in the low and intermediate fields depends on the composition (Figure 8b). In particular, $hM_3$ exhibits the highest apparent modulus at low $B$, whereas $hM_1$ is the softest. At higher fields, the modulus values of the three membranes become closer and all samples show a pronounced stiffening tendency.

A useful interpretation is that, at low to intermediate $B$, the magnetic attraction between CI-derived dipoles is partially balanced by the elastic constraint of the cotton-fiber scaffold (and, at higher $\mu$Fe loading, by the additional fibrous oxide network). In this regime, the membrane can exhibit a weak plateau or non-monotonic evolution of the apparent modulus because further dipole approach and chain compaction are mechanically constrained. At higher fields, dipolar interactions become strong enough to overcome these constraints, enabling denser field-aligned structures and producing the observed high-field stiffening. This means that the magnetic field affects not only the dielectric response but also the apparent resistance of the membranes to further compression. This behavior is consistent with bulk magneto-mechanical, magnetic-field-induced stiffening, which increases resistance to deformation as magnetic interactions grow [34]. The higher initial modulus of $hM_3$ further suggests that increasing $\mu$Fe loading stiffens the membrane even before strong field-induced structuring is established.

At the same time, the non-monotonic behavior observed for $hM_2$ and especially for $hM_3$ in the low-to-intermediate field range indicates that the apparent mechanical response is more complex than a simple monotonic stiffening law. This feature may reflect competition among magnetic interactions, the pre-existing constraints imposed by the cotton scaffold, and the additional constraint introduced by the $\mu$Fe phase.

### *4.4. Validity and Limitations*

$\varepsilon_r$ is an apparent quantity obtained for a heterogeneous dielectric layer composed of cotton fibers, silicone oil, CI microparticles, and $\mu$Fe microfibers [35]. Therefore, it represents an effective device-level response rather than the intrinsic permittivity of a uniform material. $e_{zz}$ is inferred from the capacitance variation under the assumption that the main geometric change occurs along the thickness direction and that the electrode area remains unchanged. In addition, $\tau_{zz}$ is estimated from a simplified dipolar model that does not explicitly account for the detailed morphology of the textile scaffold or the $\mu$Fe network. Consequently, the $E$ obtained from Equation (9) describes the relative evolution of the membrane response under a magnetic field within the framework used here.

### *4.5. Implications for Flexible Capacitive Elements*

From an application perspective, the membrane response can be tuned through composition. The preferred composition depends on whether magnetic sensitivity or mechanical constraint is the main requirement. The membrane without added $\mu$Fe, $hM_1$, exhibits the largest magnetic-field-induced capacitance change, the highest $\varepsilon_r$ and the largest magnetocapacitance. This makes it the most favorable composition when a strong magnetic-field-dependent electrical response is the main objective.

 doi:10.20944/preprints202603.1836.v1



Increasing the loading of $\mu$Fe reduces the magnetocapacitive response but increases the apparent stiffness of the membrane, particularly in the low-field range. In this sense, $hM_3$ is less dielectrically responsive but exhibits a more mechanically constrained apparent response under the magnetic field. The intermediate composition $hM_2$ provides a compromise between these two tendencies. Thus, the three investigated membranes define a practical trade-off: a lower $\mu$Fe loading favors a stronger dielectric response, whereas a higher $\mu$ Fe loading favors higher apparent rigidity and lower magnetic-field-induced reconfiguration.

The pressure-response data (Figure 6b) further indicate that the electrical behavior is not governed by stimulation of the magnetic-field alone. Although all three capacitors show a measurable increase in capacitance under compressive loading, the composition dependence differs from that observed under a magnetic field: $PC_2$ provides the highest average pressure sensitivity in the investigated range, while $PC_1$ provides the strongest magnetic field-induced capacitance change. This suggests that the mechanisms controlling pressure-induced and magnetic-field-induced capacitance variations are related but not identical, and that the membrane composition can be selected according to the dominant external stimulus. In this sense, the present hybrid membranes are best viewed as composition-tunable dielectric layers for flexible capacitor-based elements with coupled magnetic-field- and pressure-dependent response.

## 5. Conclusions

Flexible hybrid CI/$\mu$Fe cotton membranes were prepared by impregnating a woven cotton scaffold with SO-based suspensions containing CI microparticles and $\mu$Fe. The resulting membranes were then used as dielectric layers in planar capacitors. The capacitor structures responded to both the magnetic field and compressive pressure (Figure 6). Over the investigated range of 0–150 mT, the capacitance increased monotonically for all three compositions, with the strongest magnetic-field-induced response observed for $PC_1$ and the weakest for $PC_3$. Under compressive loading in the range of 0–10 kPa, the capacitance also increased for all samples, while $PC_2$ showed the highest average pressure sensitivity in the tested interval.

Within the simplified analysis adopted here, the capacitance data were also used to estimate several apparent dielectric and mechanical-response parameters, including apparent relative permittivity, a capacitance-derived strain proxy, magnetic stress, and an apparent modulus-like parameter. The apparent relative permittivity increased strongly with $B$ while the capacitance-derived strain became increasingly negative. The same analysis indicated an overall increase in the apparent stiffness parameter with magnetic field. Therefore, the data indicate that increasing the $\mu$Fe content suppresses the magnetically induced capacitance change and reduces the magnitude of the apparent deformation, while shifting the response toward higher apparent stiffness, especially at low magnetic field.

In general, hybrid CI/$\mu$Fe textile membranes behave as composition-tunable dielectric layers in flexible capacitor structures that respond to both magnetic field and compressive loading. The lower $\mu$Fe loading favors a stronger magnetic-field-induced capacitance change, whereas the higher $\mu$Fe loading is associated with a more mechanically constrained apparent response. This behavior makes such soft magnetic textile composites promising candidates for multifunctional capacitor-based sensing elements. Further work should address frequency dependence, cycling stability, reversibility, and direct mechanical validation of the capacitance-derived apparent quantities.

**Author Contributions:** Conceptualization, I.B; methodology, I.B. and E.M.A.; validation, I.B. and E.M.A.; formal analysis, I.B. and E.M.A.; investigation, I.B.; data curation, I.B. and E.M.A.; writing—original draft preparation, I.B.; writing—review and editing, I.B., E.M.A., M.B., L.C. and G.P.; visualization, E.M.A.; supervision, I.B., E.M.A., M.B., L.C. and G.P.; project administration, E.M.A. All authors have read and agreed to the published version of the manuscript.

**Funding:** This research received no external funding.

**Institutional Review Board Statement:** Not applicable.

 doi:10.20944/preprints202603.1836.v1



**Informed Consent Statement:** Not applicable.

**Data Availability Statement:** The data supporting the findings of this study are available within the article.

**Acknowledgments:** The authors are grateful to Dr. Paula Sfirloaga for providing SEM and EDX data for cotton fabric and hybrid membranes.

**Conflicts of Interest:** The authors declare no conflicts of interest.

## Appendix A. Morphological and Magnetic Characterization of CI Microparticles

SEM image of CI microparticles confirms the nearly spherical morphology, with a mean diameter of approximately 5 µm (Figure A1a), while the magnetization curve shows a much stronger magnetic response than that of the $\mu$Fe microfibers. Specific magnetization as a function of magnetic field intensity, indicating saturation at approximately 195 A·m$^2$/kg for $H \approx 600$ kA/m. The substantially larger saturation magnetization of CI, compared with that of the $\mu$Fe microfibers (see details in Ref. [24]), supports its role as the primary magnetic filler in the hybrid membranes.

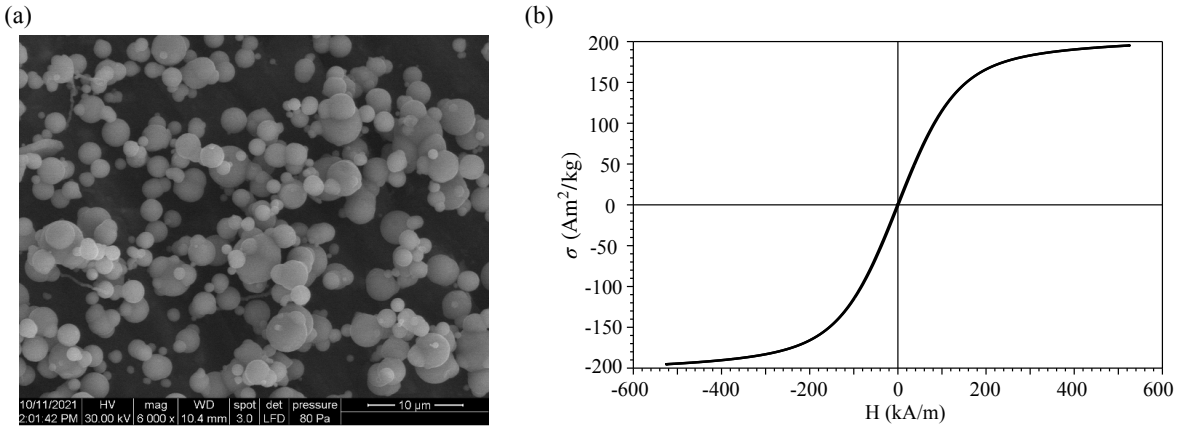


**Figure A1.** Supplementary characterization of the CI microparticles used in the present work. (a) SEM image. (b) Magnetization curve (obtained with an experimental setup described in Ref. [36]).

## Appendix B. Hysteresis Under Magnetic-Field Cycling

Figure A2 shows the hysteretic dependence of the capacitance on $B$ for the three planar capacitors $PC_1$–$PC_3$. In all cases, the capacitance increases monotonically with increasing $B$, while during the reverse sweep the capacitance remains higher than on the forward branch at the same value of $B$. This behavior demonstrates a clear hysteretic magnetocapacitive response and indicates that the field-induced internal microstructure formed inside the hybrid CI/$\mu$Fe membranes is only partially reversible when the magnetic field is reduced.

The hysteresis effect is most pronounced for $PC_1$, decreases for $PC_2$, and is weakest for $PC_3$, which is consistent with the corresponding reduction in the overall magnetic-field-induced capacitance variation. Overall, these results show that the capacitor response is not only magnetically tunable, but also exhibits a measurable memory effect associated with the progressive formation and partial persistence of the internal field-induced structure.

 doi:10.20944/preprints202603.1836.v1



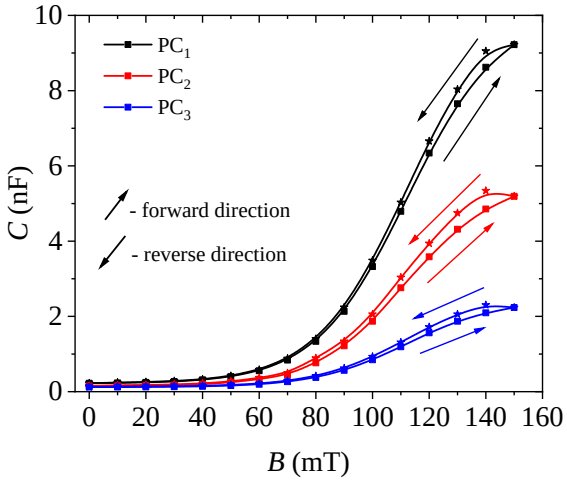


**Figure A2.** Hysteresis of the capacitance response as a function of $B$ for the three planar capacitors $PC_1$, $PC_2$, and $PC_3$. The magnitude of the hysteresis is highest for $PC_1$, intermediate for $PC_2$, and lowest for $PC_3$. Points - experimental data. Continuous lines - interpolation.

## References


1. Su, M.; Li, P.; Liu, X.; Wei, D.; Yang, J. Textile-Based Flexible Capacitive Pressure Sensors: A Review. *Nanomaterials* **2022**, *12*. https://doi.org/10.3390/nano12091495.
2. Vu, C.C.; Kim, J. Highly elastic capacitive pressure sensor based on smart textiles for full-range human motion monitoring. *Sens. Actuat. A* **2020**, *314*, 112029. https://doi.org/10.1016/j.sna.2020.112029.
3. Mathew, S.; Chintagumpala, K. A review of recent progress in flexible capacitance pressure sensors: materials design, printing methods, and applications. *Adv. Compos. Hybrid Mater* **2025**, *8*, 236. https://doi.org/10.1007/s42114-025-01304-2.
4. Ko, Y.; Vu, C.C.; Kim, J. Carbonized Cotton Fabric-Based Flexible Capacitive Pressure Sensor Using a Porous Dielectric Layer with Tilted Air Gaps. *Sensors* **2021**, *21*. https://doi.org/10.3390/s21113895.
5. Masihi, S.; Panahi, M.; Maddipatla, D.; Hanson, A.J.; Bose, A.K.; Hajian, S.; Palaniappan, V.; Narakathu, B.B.; Bazuin, B.J.; Atashbar, M.Z. Highly Sensitive Porous PDMS-Based Capacitive Pressure Sensors Fabricated on Fabric Platform for Wearable Applications. *ACS Sensors* **2021**, *6*, 938–949. PMID: 33728910, https://doi.org/10.1021/acssensors.0c02122.
6. Semisalova, A.S.; Perov, N.S.; Stepanov, G.V.; Kramarenko, E.Y.; Khokhlov, A.R. Strong magnetodielectric effects in magnetorheological elastomers. *Soft Matter* **2013**, *9*, 11318–11324. https://doi.org/10.1039/C3SM52523F.
7. Cvek, M.; Jamatia, T.; Suly, P.; Urbanek, M.; Torres-Mendieta, R. Stable Magnetorheological Fluids Containing Bidisperse Fillers with Compact/Mesoporous Silica Coatings. *Int. J. Mol. Sci.* **2022**, *23*. https://doi.org/10.3390/ijms231911044.
8. Bunoiu, O.M.; Bica, I.; Anitas, E.M.; Chirigiu, L.M.E. Magnetodielectric and Rheological Effects in Magnetorheological Suspensions Based on Lard, Gelatin and Carbonyl Iron Microparticles. *Materials* **2024**, *17*. https://doi.org/10.3390/ma17163941.
9. Kostrov, S.A.; Shamonin, M.; Stepanov, G.V.; Kramarenko, E.Y. Magnetodielectric Response of Soft Magnetoactive Elastomers: Effects of Filler Concentration and Measurement Frequency. *Int. J. Mol. Sci.* **2019**, *20*. https://doi.org/10.3390/ijms20092230.
10. Stepanov, G.V.; Bakhtiiarov, A.V.; Lobanov, D.A.; Borin, D.Y.; Semerenko, D.A.; Storozhenko, P.A. Magnetoresistive and magnetocapacitive effects in magnetic elastomers. *SN Appl. Sci.* **2022**, *4*, 178. https://doi.org/10.1007/s42452-022-05068-y.
11. Arslan Hafeez, M.; Usman, M.; Umer, M.A.; Hanif, A. Recent Progress in Isotropic Magnetorheological Elastomers and Their Properties: A Review. *Polymers* **2020**, *12*. https://doi.org/10.3390/polym12123023.
12. Wu, X.; Guo, Y.; Tian, Z.; Li, H.; Shi, Z. Preparation and Performance Evaluation of a High Temperature Stable Magnetorheological Fluid with Shear-Thinning Resistance. *Materials* **2025**, *18*. https://doi.org/10.3390/ma18163840.
13. Choi, S.B. Sedimentation Stability of Magnetorheological Fluids: The State of the Art and Challenging Issues. *Micromachines* **2022**, *13*. https://doi.org/10.3390/mi13111904.

 doi:10.20944/preprints202603.1836.v1




14. Mordina, B.; Tiwari, R.K.; Setua, D.K.; Sharma, A. Superior elastomeric nanocomposites with electrospun nanofibers and nanoparticles of CoFe2O4 for magnetorheological applications. *RSC Adv.* **2015**, *5*, 19091–19105. https://doi.org/10.1039/C5RA00537J.
15. Pu, J.; Li, H.; Liu, J.; K., L.; Tao, X. Vector-stimuli-responsive magnetorheological fibrous materials. *Natue* **2022**, *647*, 375–382. https://doi.org/10.1038/s41586-025-09706-4.
16. Piao, S.H.; Bhaumik, M.; Maity, A.; Choi, H.J. Polyaniline/Fe composite nanofiber added softmagnetic carbonyl iron microsphere suspension and its magnetorheology. *J. Mater. Chem. C* **2015**, *3*, 1861–1868. https://doi.org/10.1039/C4TC02491E.
17. Bica, I.; Anitas, E.M.; Chirigiu, L. Hybrid Magnetorheological Composites for Electric and Magnetic Field Sensors and Transducers. *Nanomaterials* **2020**, *10*. https://doi.org/10.3390/nano10102060.
18. Kuzhir, P.; Gomez-Ramírez, A.; Lopez-Lopez, M.; Bossis, G.; Zubarev, A. Non-linear viscoelastic response of magnetic fiber suspensions in oscillatory shear. *J. Non-Newton. Fluid Mech.* **2011**, *166*, 373–385. https://doi.org/10.1016/j.jnnfm.2011.01.008.
19. Wang, Y.; Wang, M.; Gao, P.; Yu, T.; Xi, J. Discrete fiber skeleton strengthened magnetorheological grease and a novel H–B model based on fiber parameters. *AIP Advances* **2024**, *14*, 035212. https://doi.org/10.1063/5.0190591.
20. Zhao, B.; Dong, Z.; Cong, H. A wearable and fully-textile capacitive sensor based on flat-knitted spacing fabric for human motions detection. *Sens. Actuat. A* **2022**, *340*, 113558. https://doi.org/10.1016/j.sna.2022.113558.
21. Ye, X.; Tian, M.; Li, M.; Wang, H.; Shi, Y. All-Fabric-Based Flexible Capacitive Sensors with Pressure Detection and Non-Contact Instruction Capability. *Coatings* **2022**, *12*. https://doi.org/10.3390/coatings12030302.
22. Dandegaonkar, G.; Ahmed, A.; Sun, L.; Adak, B.; Mukhopadhyay, S. Cellulose based flexible and wearable sensors for health monitoring. *Mater. Adv.* **2022**, *3*, 3766–3783. https://doi.org/10.1039/d1ma01210j.
23. Xiao, Y.; Hu, H.; Guo, D.; Tong, Y.; Guo, X.; Yang, L. A jet printing highly sensitive cotton/MWCNT fabric-based flexible capacitive sensor. *Sens. Actuat. A* **2023**, *351*, 114152. https://doi.org/10.1016/j.sna.2023.114152.
24. Bica, I.; Anitas, E.M.; Choi, H.J.; Sfirloaga, P. Microwave-assisted synthesis and characterization of iron oxide microfibers. *J. Mater. Chem. C* **2020**, *8*, 6159–6167. https://doi.org/10.1039/C9TC05687D.
25. Bica, I.; Anitas, E. Magnetic field intensity effect on electrical conductivity of magnetorheological bio-suspensions based on honey, turmeric and carbonyl iron. *J. Ind. Eng. Chem.* **2018**, *64*, 276–283. https://doi.org/10.1016/j.jiec.2018.03.025.
26. Siliconi Commerciale S.p.A. FLUIDO MS 100 Silicone Oil. https://www.siliconi.it/en/products/aerosols-production/lubricants-and-greases/silicone-oil-fluido-ms100. Accessed on 16 February 2026.
27. Iacobescu, G.E.; Bunoiu, M.; Bica, I.; Sfirloaga, P.; Chirigiu, L.M.E. A Cotton Fabric Composite with Light Mineral Oil and Magnetite Nanoparticles: Effects of a Magnetic Field and Uniform Compressions on Electrical Conductivity. *Micromachines* **2023**, *14*. https://doi.org/10.3390/mi14061113.
28. Bica, I.; Iacobescu, G.E.; Chirigiu, L.M.E. Magneto-Tactile Sensor Based on a Commercial Polyurethane Sponge. *Nanomaterials* **2022**, *12*. https://doi.org/10.3390/nano12183231.
29. Iacobescu, G.E.; Bica, I.; Chirigiu, L.M.E. Physical Mechanisms of Magnetic Field Effects on the Dielectric Function of Hybrid Magnetorheological Suspensions. *Materials* **2021**, *14*. https://doi.org/10.3390/ma14216498.
30. Moucka, R.; Sedlacik, M.; Cvek, M. Dielectric properties of magnetorheological elastomers with different microstructure. *Appl. Phys. Lett.* **2018**, *112*, 122901. https://doi.org/10.1063/1.5021750.
31. Isaev, D.; Semisalova, A.; Alekhina, Y.; Makarova, L.; Perov, N. Simulation of Magnetodielectric Effect in Magnetorheological Elastomers. *Int. J. Mol. Sci.* **2019**, *20*. https://doi.org/10.3390/ijms20061457.
32. Roghani, M.; Romeis, D.; Saphiannikova, M. Effect of microstructure evolution on the mechanical behavior of magneto-active elastomers with different matrix stiffness. *Soft Matter* **2023**, *19*, 6387–6398. https://doi.org/10.1039/D3SM00906H.
33. Munteanu, A.; Plachy, T.; Munteanu, L.; Ngwabebhoh, F.A.; Stejskal, J.; Trchova, M.; Kubik, M.; Sedlacik, M. Bidisperse magnetorheological fluids utilizing composite polypyrrole nanotubes/magnetite nanoparticles and carbonyl iron microspheres. *Rheol. Acta* **2023**, *62*, 461–472. https://doi.org/10.1007/s00397-023-01409-9.
34. Salim, N.J.; Arretche, I.; Matlack, K.H. Magnetic field induced toughening mechanisms in isotropic and anisotropic soft magnetoactive elastomers. *Extreme Mech. Lett.* **2025**, *78*, 102368. https://doi.org/10.1016/j.eml.2025.102368.

 doi:10.20944/preprints202603.1836.v1



35. Stepanov, G.; Bakhtiiarov, A.; Lobanov, D.; Storozhenko, P. Magnetoresistivity and piezoresistivity of magnetoactive elastomers. *J. Magn. Magn. Mater.* **2023**, *587*, 171313. https://doi.org/10.1016/j.jmmm.2023.171313.
36. Ercuta, A. Sensitive AC Hysteresigraph of Extended Driving Field Capability. *IEEE Trans. Instrum. Meas.* **2020**, *69*, 1643–1651. https://doi.org/10.1109/TIM.2019.2917237.